Nanovoid growth in BCC -Fe: influences of initial void geometry

Nanovoid growth in BCC α-Fe: influences of initial void geometry

Shuozhi Xu[1] and Yanqing Su[2]

[1] GWW School of Mechanical Engineering, Georgia Institute of Technology, Atlanta, GA 30332-0405, USA
[2] School of Earth and Atmospheric Sciences, Georgia Institute of Technology, Atlanta, GA 30332-0340, USA

E-mail: shuozhixu@gatech.edu

Abstract

The growth of voids has a great impact on the mechanical properties of ductile materials by altering their microstructures. Exploring the process of void growth at the nanoscale helps in understanding the dynamic fracture of metals. While some very recent studies looked into the effects of the initial geometry of an elliptic void on the plastic deformation of face-centered cubic metals, a systematic study of the initial void ellipticity and orientation angle in body-centered cubic (BCC) metals is still lacking. In this paper, large scale molecular dynamics simulations with millions of atoms are conducted, investigating the void growth process during tensile loading of metallic thin films in BCC α-Fe. Our simulations elucidate the intertwined influences on void growth of the initial ellipticity and initial orientation angle of the void. It is shown that these two geometric parameters play an important role in the stress–strain response, the nucleation and evolution of defects, as well as the void size/outline evolution in α-Fe thin films. Results suggest that, together with void size, different initial void geometries should be taken into account if a continuum model is to be applied to nanoscale damage progression.

Keywords: molecular dynamics, metals, voids, geometry, deformation

(Some figures may appear in colour only in the online journal)

1. Introduction

The growth of voids plays a significant role in mechanical properties of metals in various types of environments at different length scales [1]. On the one hand, voids can grow and deform in strained ductile materials, especially in the presence of a large stress triaxiality, before coalescing with each other to form cracks which then propagate and grow, eventually resulting

in macroscopic failure [2]. On the other hand, even without the subsequent crack formation, the voids can impede the motion of dislocations, and lead to a higher resolved shear stress for dislocations to bypass larger voids [3]. For example, in nuclear power systems, the metallic components of reactors are bombarded by a flux of fast neutrons, which increase the yield stress, reduce the work hardening rate and ductility, and promote flow localization by dislocation channeling [4, 5]. During the growth of voids, defects (e.g. dislocations, twins) emission and phase transformation at the void surface, which are important in void deformation, occur at the nanoscale [6, 7]. This renders continuum-based approaches (e.g. the finite element method [8–11]) inappropriate for nanovoid growth study. Alternatively, atomistic simulations such as molecular dynamics (MD), which explicitly provide the trajectory of every atom, have attracted a lot of attention and been widely employed to probe the issue of nanovoid growth in the last decade [12–14].

Most MD simulations so far, however, have been conducted in face-centered cubic (FCC) systems such as Cu [15–17], Ni [18], and Al [19]. Void growth in other types of lattice, e.g. body-centered cubic (BCC), is less explored due to some challenges in modelling their lattice defects [20]. One challenge is the difficulty of the semi-empirical potentials to accurately predict the energy barrier of the dislocation kink formation, which controls the plasticity in BCC metals at low temperatures [21]. Another challenge in BCC is the complication that the screw dislocation cross-slip is interwined with the kink-pair formation during the dislocation glide [22], the possible {1 1 2} slip traces between {1 1 0} slip planes [23], and the less well defined slip planes (than FCC) because of the compact dislocation core [24]. In spite of these challenges, progress has been made by researchers. Xu *et al* [25] investigated the effects of strain rate, initial porosity, and specimen size in void growth in BCC vanadium. Rudd [26] explored void growth in five BCC metals and found that plastic deformation is dominated by twinning and dislocation emission, respectively, at higher and lower strain rates. Tang *et al* [27] similarly reported such a slip-to-twinning transition as the strain rate increases, in a voided BCC Ta model subject to a uniaxial tensile strain or a hydrostatic tensile loading; their MD simulations also revealed a special type of dislocation shear loop at the void surface that can expand as partial or perfect dislocations, evolving into prismatic loops through reaction with each other or developing into twins [28]. However, the atomic-scale mechanisms of the effects of the initial void geometry in nanovoid growth, which have recently been explored in FCC metals [16, 19, 29], remain largely unknown in BCC metals.

In this paper, large scale MD simulations with more than ten million atoms are performed to systematically study the effects of (i) the initial void ellipticity and (ii) the initial void orientation angle in deformed thin films of α-Fe (a highly elastically anisotropic metal), with up to 20% uniaxial strain. Emphasis will be placed on how these two factors influence the stress–strain response, the defect formation, and the void size/outline evolution.

2. Methodology

Figure 1 presents the simulation cell for nanovoid growth, oriented with x[1 0 0], y[0 1 0], and z[0 0 1]. Periodic boundary conditions (PBCs) are applied along all three axes to simulate a periodic array of voids in an infinite system. A void, whose cross-sectional area on the y-z plane has an initial ellipticity $e = \sqrt{(a^2 - c^2)/a^2}$, is positioned in the center of the model with its centroid direction throughout the specimen along the x axis, where a and c are the lengths of the void major and minor axes respectively. The initial orientation angle θ is formed between the void major axis and the y axis, where $\theta \leqslant 90°$, as illustrated in figure 1(b). In our simulations, e varies from 0 (circle), 0.2, 0.4, 0.6, to 0.8 by adjusting a and c, while θ varies from 0°,
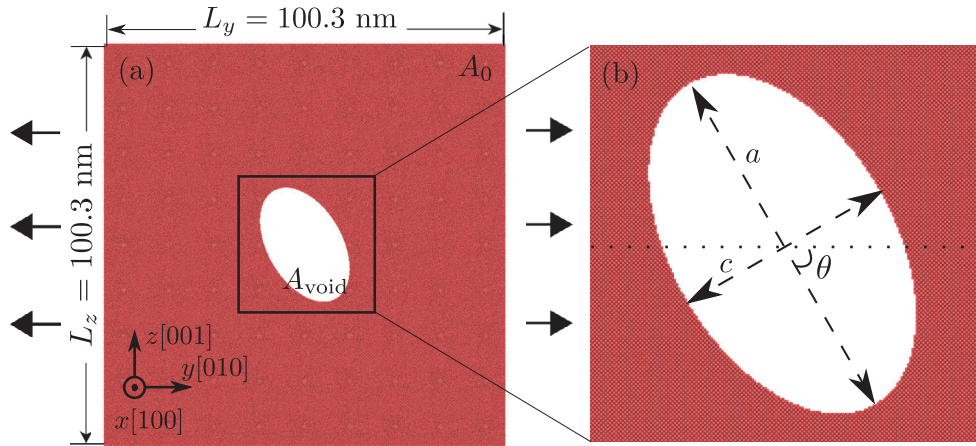
Figure 1. Simulation cell of a metallic thin film containing a void. Depth of the model in one supercell $L_x = 15.1$ nm. a and c are the length of the void major and minor axes, respectively. The orientation angle θ is formed between the void major axis and the y axis, where $\theta \leqslant 90°$. $A_0 = L_y L_z$ is the initial simulation cell area and A_{void} is the cross-sectional area of the void, both of which are on the y-z plane.

$15°, 30°, 45°, 60°, 75°$ to $90°$. Irrelevant to the values of e and θ, the initial cross-sectional area of the void on the y-z plane is $\pi a c = 144\pi$ nm^2. The simulation cell has an initial size of 15.1 nm (L_x) by 100.3 nm (L_y) by 100.3 nm (L_z) along the x, y, and z directions respectively, resulting in an initial void area fraction on the y-z plane of about 4.4%. The lattice parameter is 2.8553 Å, and each cell contains about 12.47 million atoms.

The embedded-atom method (EAM) potential of Proville *et al* [30] is adopted to describe the interactions between α-Fe atoms because it accurately predicts the Peierls barrier, hard dislocation core energy, and straight dislocation trajectory between two easy dislocation cores [31]. All atomisitc simulations are carried out using LAMMPS [32]. After a void is formed by removing atoms within a specified shape on the y-z plane, energy minimization using a conjugate gradient algorithm is performed to attain the minimum energy configuration. It follows that the dynamic relaxation is conducted for 20 ps to reach an equilibrium state, after which a uniaxial homogeneous deformation is applied along the y direction at a strain rate of 10^9 s^{-1}. In all dynamic simulations, a Velocity Verlet algorithm with a time step of 2 fs is employed to update the atomic positions, and a Nosé–Hoover NPT integrator is used to maintain a constant temperature of 10 K. The simulation results are only slightly affected by changing the time step, as dicussed in appendix A. During the tensile loading along the y direction, both L_x and L_z are allowed to vary to let the normal stresses along the x and z axes vanish, and the void area fraction f on the y-z plane at $x = L_x/2$ is calculated, equaling A_{void}/A, where A_{void} and A are the areas of the void and the simulation domain respectively (figure 1(a)). Simulation results are visualized using OVITO [33], which uses adaptive common neighbor analysis (a-CNA) [34] to identify the local atomic structures. The void area is calculated through surface recognition instead of counting defected volume inside the void; the Matlab code for this is publicly available [35]. Some runs were completed using comet and bridges on Extreme Science and Engineering Discovery Environment (XSEDE) [36].
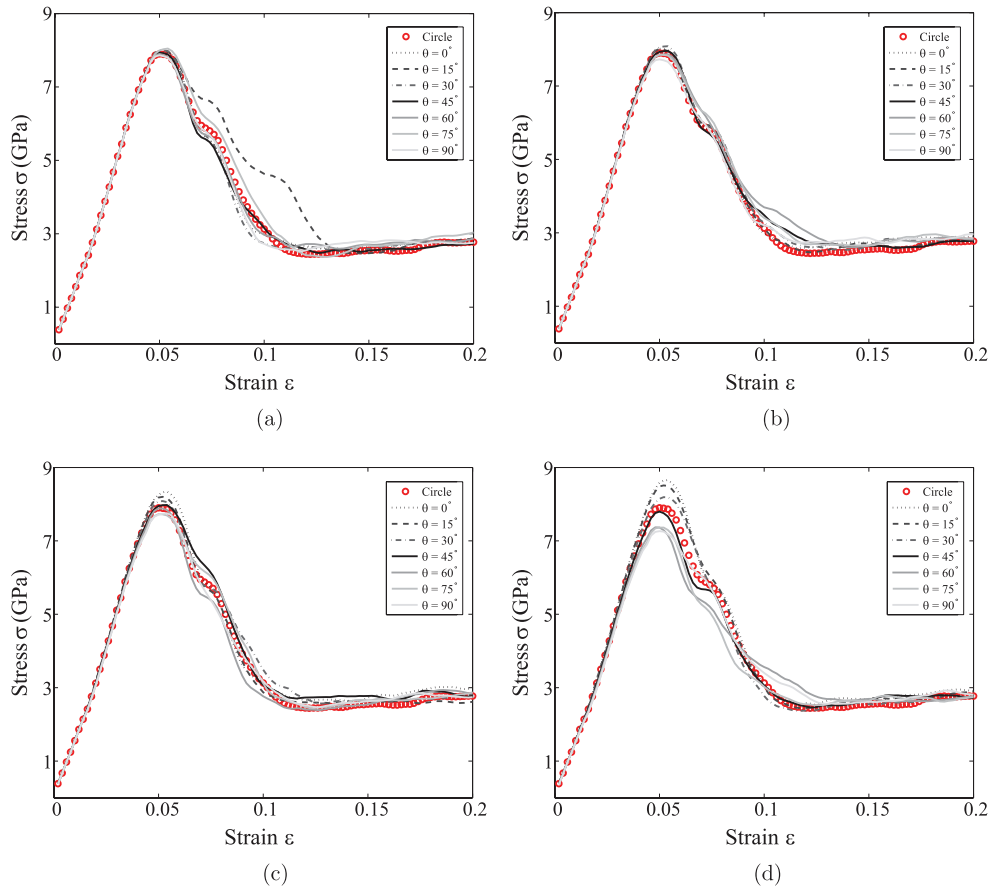
3

Figure 2. Stress–strain curves for different initial void ellipticity (a) $e = 0.2$, (b) $e = 0.4$, (c) $e = 0.6$, and (d) $e = 0.8$ in cases of different orientation angle θ.

3. Results and discussion

In this section, we analyze and discuss the stress–strain response (section 3.1), the defect nucleation and evolution (section 3.2), as well as the void area fraction and void outline evolution in the nanovoid growth (section 3.3), when different initial void ellipticity and void orientation angle are considered.

3.1. Stress–strain response

The normal stress along the *y* axis with respect to the uniaxial strain along the same direction are plotted in figure 2 for different initial ellipticity *e* and initial orientation angle θ, where the case of a circular void is used as a reference in all subplots. The residual normal stress along the *y* direction in the undeformed model ($\varepsilon = 0$) immediately before the tensile loading is about 100 MPa, which is negligible compared with the maximum uniaxial stress of about 8 GPa. Note that all curves begin with $\varepsilon = 0.002$. In all simulations, the initial defect nucleation from the void surface, corresponding to which we denote σ_Y as the yield stress, is always prior to the point with the maximum stress. It is found that (1) both the slope of the stress–strain curve prior to the yield point and the flow stress are roughly the same for different *e* and θ, indicating that
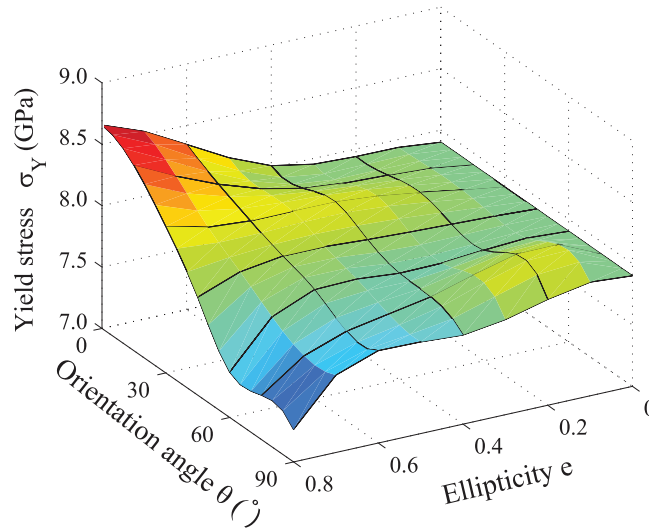
Figure 3. Yield stress σ_Y as a function of both initial ellipticity e and initial orientation angle θ.

the Young's modulus at the elastic stage is invariant with respect to these two factors, and (2) the influence of θ on σ_Y is more pronounced in the case of a larger e because, geometrically, a more elliptic void differs more from the circle and thus the effect of θ is more noticeable. Also note that the strain corresponding to the yield stress is the same with varying e and θ, which is in contrast with the FCC metal [16].

To further analyze the dependence of σ_Y on the initial ellipticity e and the initial orientation angle θ, we plot the yield stress σ_Y as a function of e and θ in figure 3. The general trend is that for a fixed e, a larger θ would lead to a smaller σ_Y, while for a different θ the effect of e on σ_Y varies. Specifically, for a small angle, e.g. $\theta \leqslant 30°$, a larger e results in a higher σ_Y; for a large angle, e.g. $\theta \geqslant 60°$, a larger e is accompanied by a lower σ_Y; for an intermediate angle, e.g. $\theta = 45°$, the variation of e takes little effect on the stress–strain response. This is because on the one hand, as will be discussed later in section 3.2, defects always start to nucleate from the top and bottom sides of the void, which have the largest stress concentrations in the specimen; on the other hand, for elliptic voids ($e > 0$), a larger θ results in a larger curvature of the void's cross-sectional area on the y-z plane at its top/bottom sides, which further intensifies the stress concentrations at these sites and thus advances the yield point and lowers σ_Y. From the perspective of damage mechanics, in the case of a small θ, the effective stress along the y axis is decreased by a smaller cross-sectional area of the void on the mid x-z plane [2], thus the material yields at a higher far field stress, which agrees with our MD simulations.

3.2. Defect nucleation and evolution

In this section, we discuss in detail the defect nucleation and evolution near the surface of a void of initial circular shape ($e = 0$, figure 4) and of an elliptic shape ($e = 0.8$) with three different initial orientation angles $\theta = 0°$ (figure 5), 45° (figure 6), and 90° (figure 7). These four voids are chosen to represent a complete set of e and θ.

For the circular void (figure 4), at a small uniaxial strain ($\varepsilon < 0.04$), the simulation cell expands elastically, and is free of any lattice defects except the void itself. At $\varepsilon = 0.04$ (figure 4(a)), a compact slip band begins to nucleate at both the top and bottom sides of the void. The
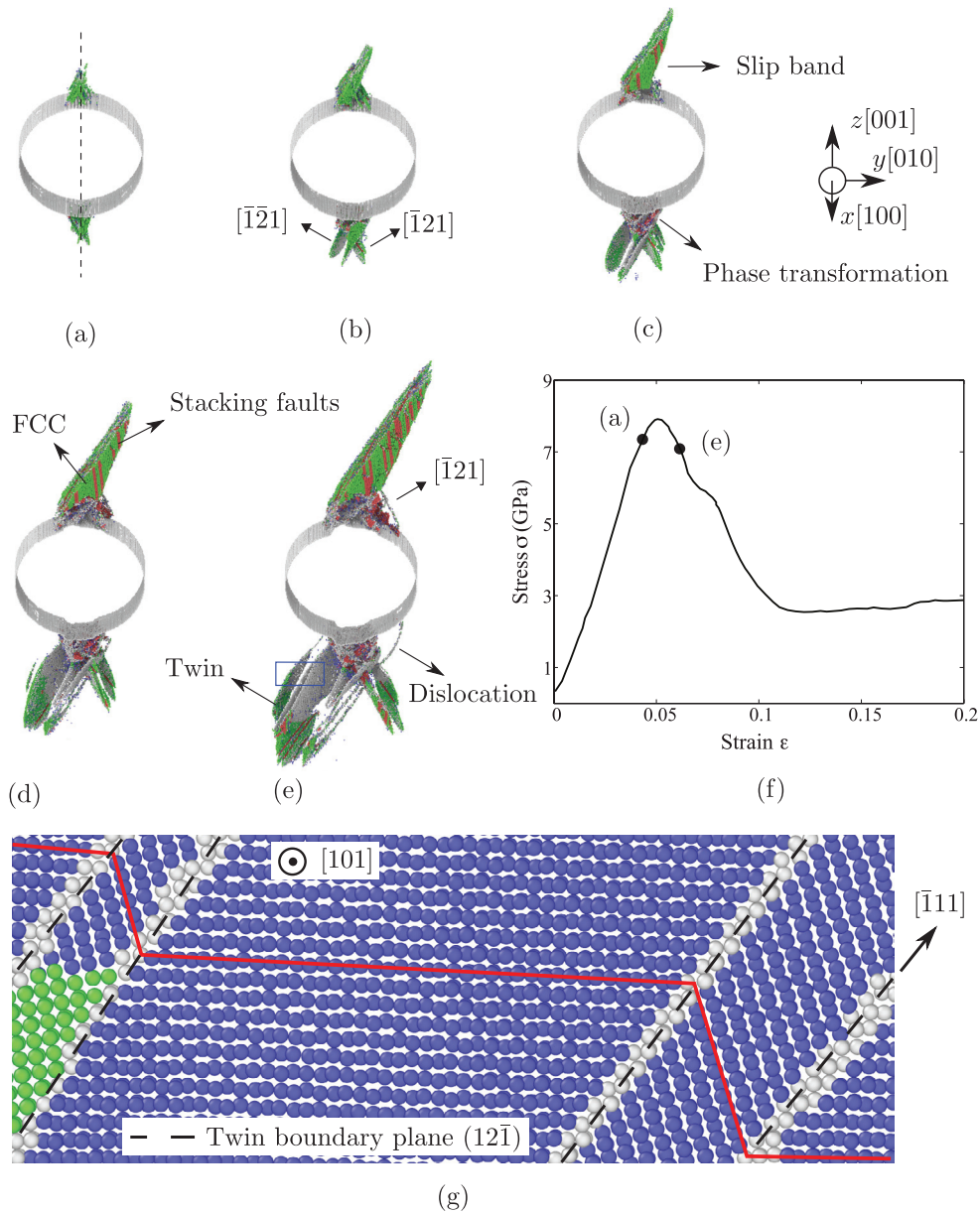
Figure 4. Snapshots of defect nucleation and evolution at the surface of a circular void. Atoms are colored by the a-CNA [34]: green, red, blue, and white are of local FCC, HCP, BCC, and unknown structures respectively. All atoms with the centrosymmetry parameter [37] smaller than 6 are removed in (a)–(e). The same rendering method is used throughout this paper for all atomic configurations. The line of symmetry of the void with respect to the z direction is marked by a dashed line in (a). The strains corresponding to (a) and (e) are labeled in the stress–strain curve in (f). The magnified atomic configuration within the dark blue box in (e) is given in (g). (a) $\varepsilon = 0.04$. (b) $\varepsilon = 0.044$. (c) $\varepsilon = 0.048$. (d) $\varepsilon = 0.052$. (e) $\varepsilon = 0.056$.
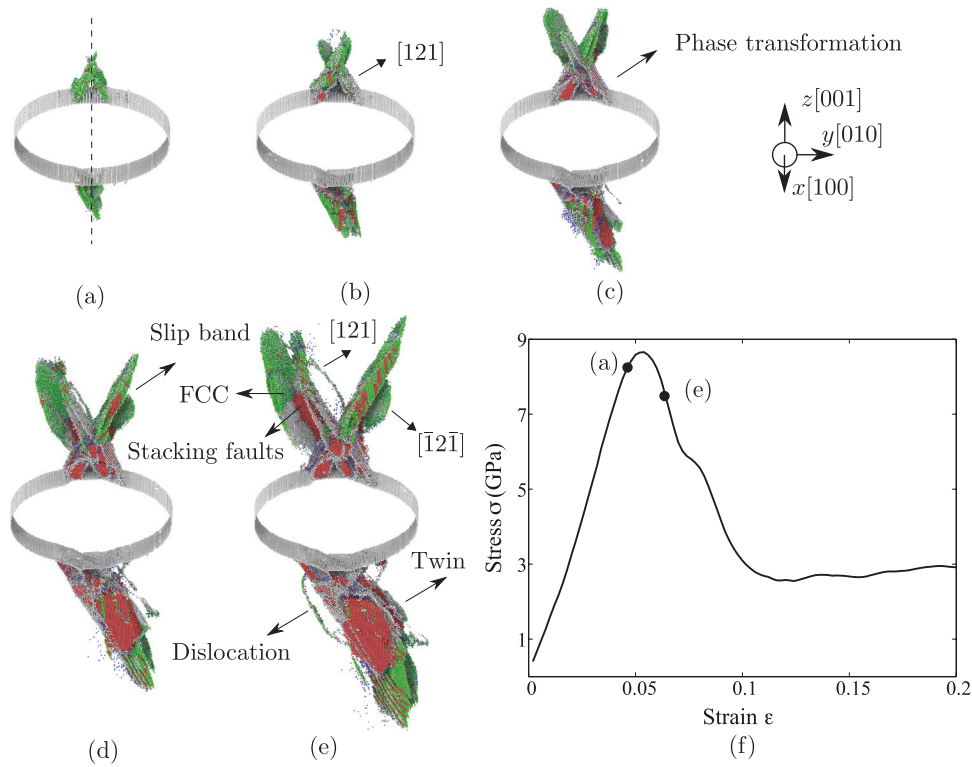
Figure 5. (a)–(e) Snapshots of defect nucleation and evolution at the surface of a void of $e = 0.8$ with $\theta = 0°$. The minor axis of the void is marked by a dashed line in (a). The strains corresponding to (a) and (e) are labeled in the stress–strain curve in (f). (a) $\varepsilon = 0.044$. (b) $\varepsilon = 0.048$. (c) $\varepsilon = 0.052$. (d) $\varepsilon = 0.056$. (e) $\varepsilon = 0.06$.

edge of the slip band consists of numerous leading partial dislocations on consecutive slip planes [38]. This slip band is manifested by BCC–FCC phase transformation, with a small energy barrier of about 0.122 eV/atom [39]. The occurance of the FCC local structures in the BCC lattice was also found at the crack tip in an α-Fe sample subject to a uniaxial deformation perpendicular to the initial crack plane [40], as well as during the straining of another BCC metal Mo [41], both at the same strain rate of $10^9\,\mathrm{s}^{-1}$ as in this work. At a larger strain of 0.044 (figure 4(b)), the slip band continues growing asymmetrically with respect to the z axis at the top side of the void; meanwhile, the trailing partial dislocations start to nucleate at the bottom side of the void, terminating the slip band and forming full dislocations on the ($\bar{1}\,2\,1$) plane. Later, at $\varepsilon = 0.048$ (figure 4(c)), hexagonal close-packed (HCP) local structures are formed near the bottom side of the void as well as inside the slip band near the top side, manifested by the intrinsic stacking faults in the FCC lattice. These stacking faults are formed as a consequence of the emission of Shockley partial dislocations from the void surface into the transitional FCC region [42]. We remark that the martensitic BCC–HCP transition is commonly observed in α-Fe under high pressure [43]. Moreover, two dislocations, gliding on the surface of top and bottom sides of the void respectively, are observed. At $\varepsilon = 0.056$ (figure 4(e)), a full dislocation starts to form at the top side of the void on ($\bar{1}\,2\,1$) plane. At the bottom side, the leading partial dislocations on the ($\bar{1}\,\bar{2}\,1$) plane emit from the void surface, transforming the stacking faults to multilayer twins and changing the local lattice orientations [44], as shown in figure 4(g). The formation of twins at larger strains agrees with the previous finding that a
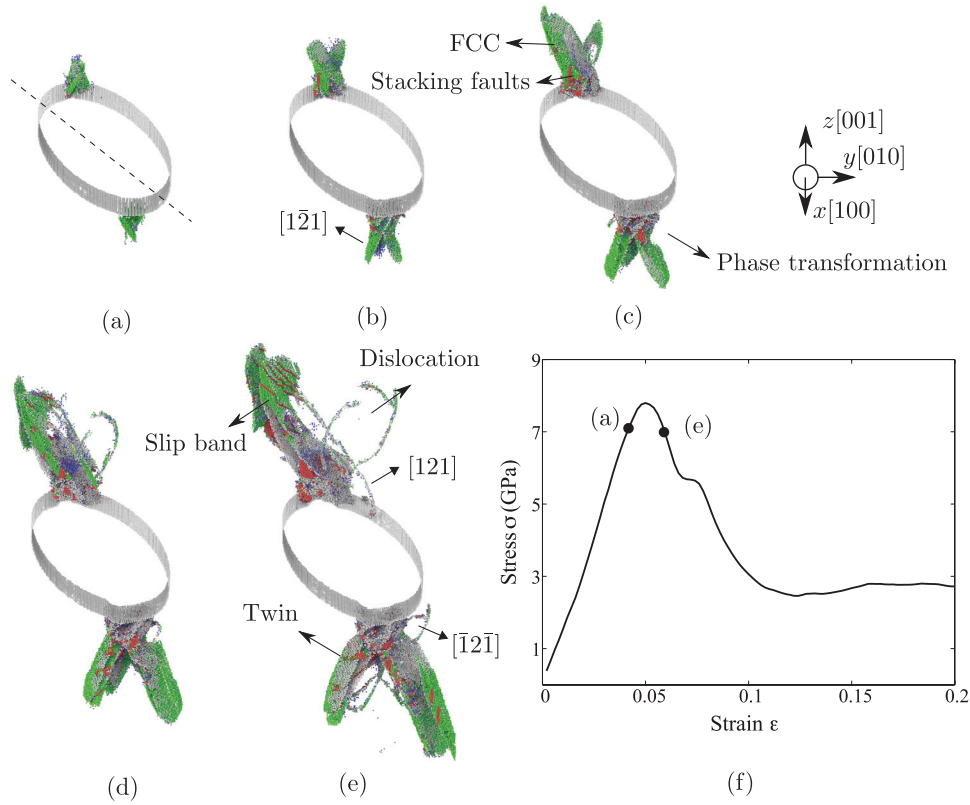
Figure 6. (a)–(e) Snapshots of defect nucleation and evolution at the surface of a void of $e = 0.8$ with $\theta = 45°$. The major axis of the void is marked by a dashed line in (a). The strains corresponding to (a) and (e) are labeled in the stress–strain curve in (f). (a) $\varepsilon = 0.04$. (b) $\varepsilon = 0.044$. (c) $\varepsilon = 0.048$. (d) $\varepsilon = 0.052$. (e) $\varepsilon = 0.056$.

higher strain rate (i.e. a higher maximum stress in the specimen) transforms the plastic mechanism from dislocation nucleation to twinning [26, 27].

Overall, a majority of defects nucleate at the top/bottom sides of the void, which is a reflection of the fact that these two sites have the highest stress concentrations in a model subject to a tensile loading along the y direction. We remark that the plastic deformation zone in α-Fe (exhibited by nucleation and evolution of slip bands, full dislocations, and twins) is much more complicated than that in FCC Cu, in which the dislocation nucleation dominates the plasticity [16]. As a result, the development of dislocation density with an increasing strain would not be a good indicator of defect evolution in this work. Also complicated in BCC metals due to the presence of multiple types of defects is the mechanism of void growth. So far, there are three dislocation-emission-based mechanisms: the first and the classical one is void growth via prismatic loop emission, which carries material away [46]; the second is that the shear loops/curves can expand and cross-slip to form a prismatic loop to grow the void [45, 47]; the third is through direct mass transport via shear loop/curve emission [17]. We remark that mass transport is associated with the formation of dislocation curves/loops but not their conservative motion. In our simulations, both prismatic and shear dislocation loops, each of which has one Burgers vector, are identified with the help of a dislocation extraction algorithm [48]. While they may contribute to the void growth, it is difficult to isolate them from other lattice defects that are also present at the void surface. Therefore, unlike FCC metals, in
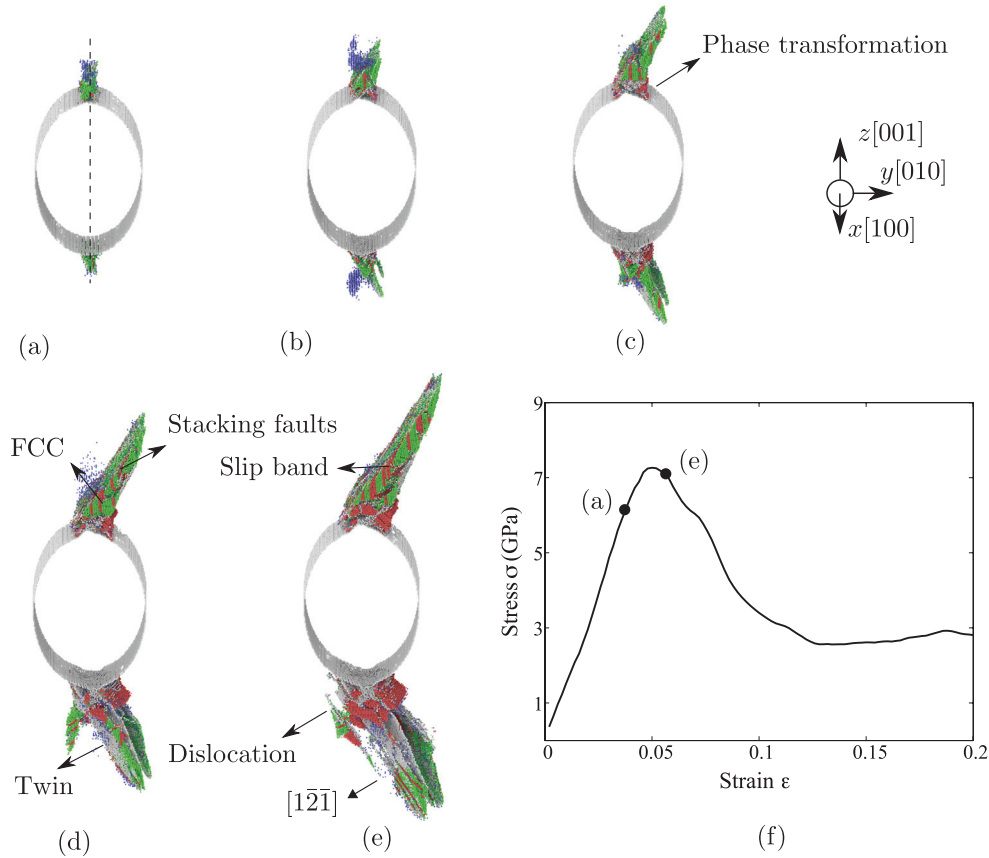
Figure 7. (a)–(e) Snapshots of defect nucleation and evolution at the surface of a void of $e = 0.8$ with $\theta = 90°$. The major axis of the void is marked by a dashed line in (a). The strains corresponding to (a) and (e) are labeled in the stress–strain curve in (f). (a) $\varepsilon = 0.048$. (b) $\varepsilon = 0.052$. (c) $\varepsilon = 0.056$. (d) $\varepsilon = 0.06$. (e) $\varepsilon = 0.064$.

which MD simulations validate the last two mechanisms, the void growth mechanism in BCC metals remains less clear and will be our future work.

For an initially elliptic void ($e > 0$), the detailed process of the defect nucleation and evolution varies with e and θ. A series of atomic configurations of defects near a void with $e = 0.8$ are shown in figure 5 ($\theta = 0°$), figure 6 ($\theta = 45°$), and figure 7 ($\theta = 90°$). In figure 5 when $\theta = 0°$, e.g. the slip bands with interior FCC atoms on (121) and ($\bar{1}\,2\,\bar{1}$) planes begin to nucleate at a strain $\varepsilon = 0.044$ (figure 5(a)). Later at $\varepsilon = 0.052$ (figure 5(c)), a large volume of BCC–HCP phase transformation occurs at the top and bottom surfaces of the void. Then at a larger strain of 0.06 (figure 5(e)), the slip bands transform to full dislocations and multilayer twins on $\{1\,1\,2\}$ slip planes. At the top surface of the void, the defects are more symmetric with respect to the z axis, compared with an initially circular void. A large amount of twins and BCC-transformed HCP local structures is present near the void top surface, where the local uniaxial stress along the y direction is higher than that for the initially circular void at the same strain of 0.06 [26, 27, 43], as shown in figure 8. The defect nucleation and evolution for $\theta = 45°$ and $90°$ are similar to those for $\theta = 0°$, except that compared with the circular void, the difference between the strain at the yield point and the strain corresponding to the maximum stress is larger for the elliptic voids when $\theta = 90°$ and smaller when $\theta = 0°$, as shown in subplots (f) of figures 4–7.
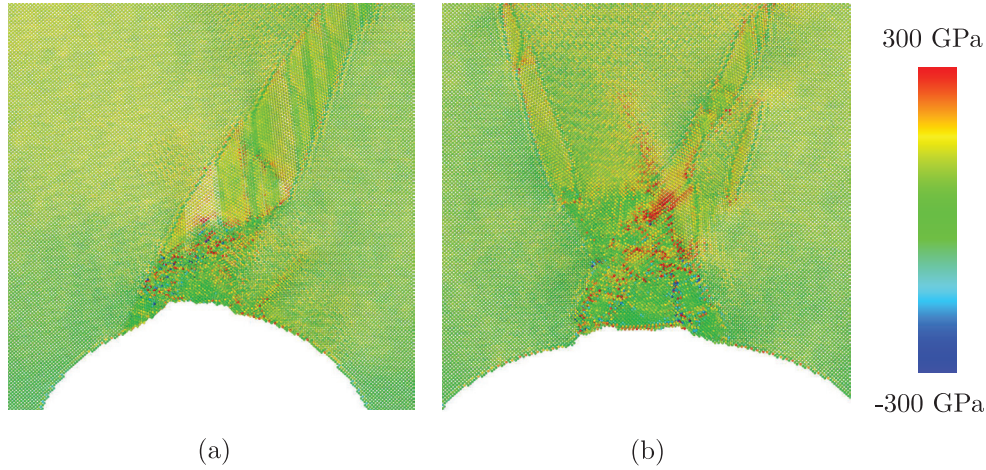
(a)　　　　　　　　　　　　　　　(b)

Figure 8. Snapshots of atoms when $\varepsilon = 0.06$ at the top side of the void of (a) initially circular shape and (b) $e = 0.8$ and $\theta = 0°$. Atoms are colored by atomic uniaxial stress along the y direction. It is found that the local stress level at the top side of the initially circular void is lower than that for the void of $e = 0.8$ and $\theta = 0°$.
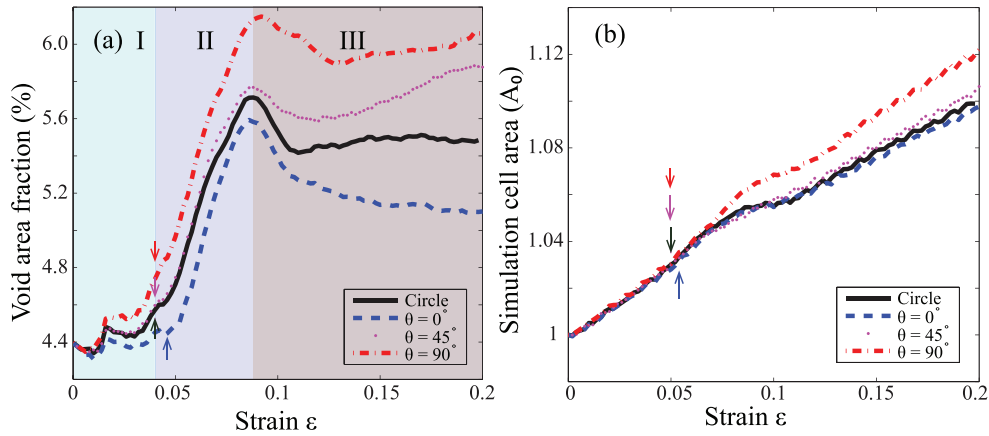

Figure 9. (a) Void area fraction f and (b) simulation cell area A as a function of strain ε for void of a circular shape ($e = 0$) and of an elliptic shape ($e = 0.8$) with three different orientation angle θ: 0°, 45°, and 90°. A_0 is the initial simulation cell area on the y-z plane. The vertical arrows mark the yield points. Based on the circular void, three regimes of void area fraction evolution are distinguished using different background colors.

For all these four voids, the defects at the void surface are asymmetric with respect to the y direction, which may be attributed to (I) the atomic-scale asperity at the void surface, which can significantly modify the defect nucleation [49], (II) the stochastic atomic trajectories in an NPT ensemble, and (III) the random atomic velocities initialization before the dynamic run; the last two causes for the asymmetry are discussed in appendix B.

3.3. Void area fraction and void outline evolution

Figure 9(a) presents the evolution of the area fraction f of the voids in figures 4–7 as a function of strain ε. Three regimes during the void growth are identified. In regime I, at a small ε,
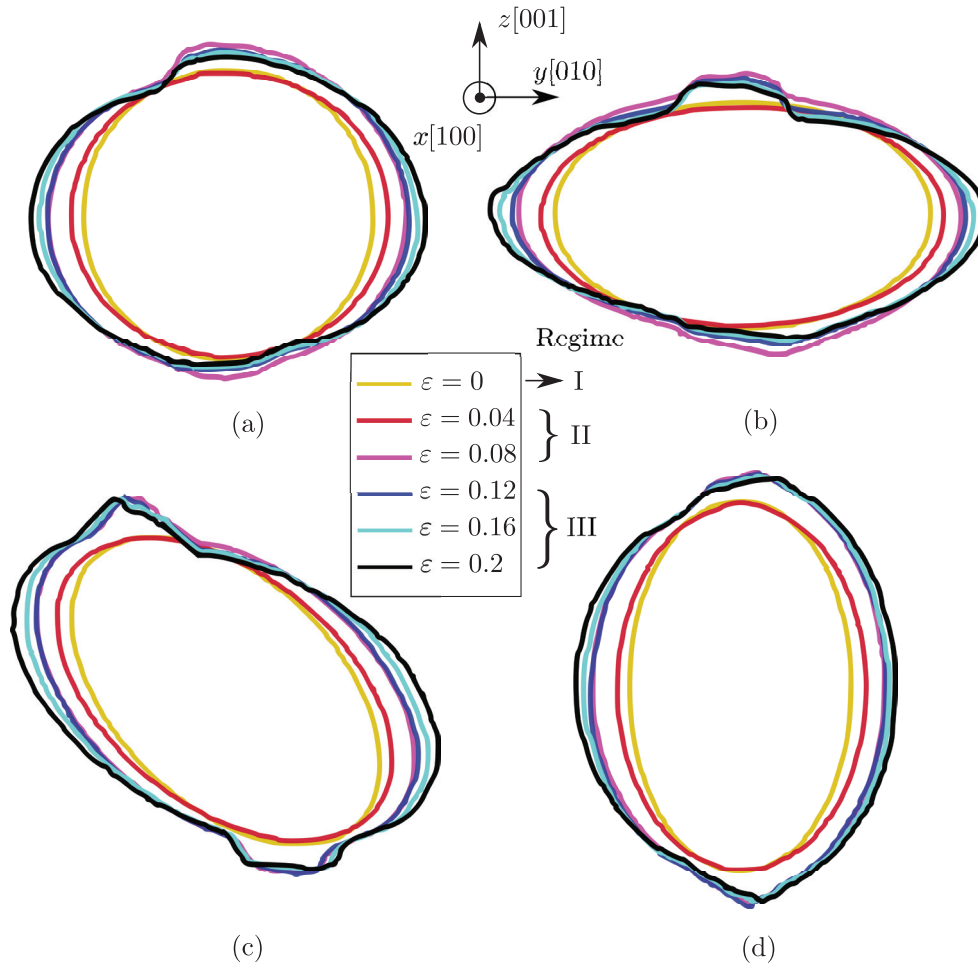
Figure 10. Outline evolution of a void with (a) a circular shape with $e = 0$ and an elliptic shape with $e = 0.8$ when (b) $\theta = 0°$, (c) $\theta = 45°$, and (d) $\theta = 90°$. Void outline measured at different strain ε is distinguished by different colors.

prior to the initial defect emission from the void surface, f varies slowly in all four cases. Then, after the yield point, e.g. at $\varepsilon = 0.04$ for a circular void, as marked by the vertical arrows in figure 9(a), regime II is initiated. In this regime, f starts to grow much faster due to the defect nucleation at the void surface that pushes some surrounding atoms outwards. Later, at $\varepsilon \approx 0.09$ for a circular void, regime III starts. In this regime, f decreases slightly before remaining largely invariant with ε. This can be explained by the dynamic balance of the atoms being pulled towards the voids and those being pushed away from the voids, i.e. the saturation of defects. For regimes II and III, all four cases have the similar onset strain, while the onset void area fraction f are different, with the elliptic void of $\theta = 0°$ having the lowest onset f. Note that among the four voids, the elliptic void with $\theta = 0°$ is the only one with a monotonically declining f after the peak. A further analysis reveals that the decrease in f is due to the void area A_{void} remaining roughly constant while the simulation area A is still increasing (figure 9(b)). In comparison, in regime III, the circular void expands at a similar pace as the simulation area A, resulting in an approximately constant f; the other two elliptic voids ($\theta = 45°$ and $90°$)

grow faster than A, leading to an increasing f. The outstanding feature in the case of $e = 0.8$ and $\theta = 0°$ is probably because its top and bottom sides are the farthest from the periodic cell boundaries normal to the z axis, which allows more room for defect development prior to the saturation; such a high defect density facilitates pulling more atoms towards the void, and so restrains the void from expanding. Also note that the onset strain for regimes II and III is the same for the four voids, which is in contrast with the FCC metal [16].

The simulation cell area A in all cases increases linearly with the applied strain ε at the same pace prior to the yield point (marked by arrows in figure 9(b)), as a result of the Poisson's ratio of α-Fe at the elastic stage $\nu = 0.29$. Then, at larger strains, in the presence of defects, the simulation cell area A in the four cases begin to differ, with the case of $e = 0.8$ and $\theta = 90°$ having the largest A, i.e. the smallest ν. This quasi-linear evolution of A with respect to ε indicates that the change in the void area fraction f is mainly due to the change of the void area A_{void}.

The outline evolutions of these four voids are displayed in figure 10. Take the circular void as an example. In regime I ($\varepsilon = 0$), the void size along the y axis increases while that along the lateral z direction slightly shrinks, in the same way as the simulation cell. In regime II ($\varepsilon = 0.04$ and 0.08), the void grows along both the y and z axes, with the latter at a slower pace, as a result of the defect nucleation and migration pushing the surrounding atoms away from the void. This bi-directional void growth corresponds to the fast increase in the void area fraction f in this regime. The void's cross-sectional area boundary becomes irregular, non-smooth in this regime. The void outline, whose top and bottom surfaces bow out, is no long symmetric with respect to the z axis, corresponding to the asymmetric defect formation as shown in figure 4. We remark that the bowing out of some part of the void outline, which is also found during crack tip blunting in α-Fe [42], was not observed in Cu for the same e and ε [16]. In regime III ($\varepsilon = 0.12, 0.16$, and 0.2), the void size increases along the y axis only, while that along the z axis shrinks; the pace of the latter is higher than that in regime I. The outline evolution of the elliptic voids ($e = 0.8$) follows a similar pattern to that of the circle, except that for $\theta = 0°$, the outline of the void at its top surface is more symmetric with respect to the z axis, as a result of the more symmetric defect formation at the same site as shown in figure 5. Also noteworthy is that the elliptic void with $\varepsilon = 90°$ has the largest onset void area fraction for regime III, related to its initial shape approaching an edge crack more than the others [50]. It is expected that with further straining beyond $\varepsilon = 0.2$, a fracture will develop around the void before expanding to 'reconnect' across the PBCs along the z axis.

4. Conclusions

In this work, we perform MD simulations with more than 12 million atoms to investigate nanovoid growth in BCC α-Fe thin films subject to large deformation up to 20%. Focus is placed on the effects of the initial void ellipticity e and the initial orientation angle θ of the void—two important factors dictating the initial void geometry—in the void growth progress. Results are summarized as follows:

  (i) The initial void geometry not only alters the stress–strain response, from a macroscopic perspective, but also affects the defect nucleation/evolution and the void size/outline evolution, from a nanoscopic perspective;

 (ii) In terms of the stress–strain response, the effect of θ is more pronounced for a larger e. The general trend is that a larger θ results in a lower yield stress σ_Y, while the effect of e on σ_Y varies with θ. When $\theta \leqslant 30°$, an increasing e is accompanied by a larger σ_Y; for $\theta \geqslant 60°$, a larger e leads to a smaller σ_Y; with an intermediate initial orientation angle, e.g.

$\theta = 45°$, the variation of e has little effect. The slope of the stress–strain curve prior to the yield point and the flow stress, however, remain the same for different e and θ;

(iii) In terms of the defect nucleation and evolution, the plastic deformation zone in α-Fe is complicated. In general, slip bands mostly composed of FCC atoms nucleate from the void surface right after the yield point, which is always prior to the point of maximum stress. At larger strains, more partial dislocations emit to form full dislocations and stacking faults, along with the phase transformation from BCC to HCP local structure. With the aid of more partial dislocations at an even higher strain, stacking faults can be transformed into multilayer twins;

(iv) Based on the void area fraction f evolution with the applied strain ε, three regimes in the void growth are identified: in regime I, prior to the yield point, f varies slowly; in regime II, defects start to nucleate from the void surface, pushing some atoms outwards, resulting in a much higher increase rate of f and a non-smooth void outline; in regime III, the variation of f decays as compared to that in regime II, due to the saturation of defects in the system. In addition, in regime III, the void size in some cases remains relatively constant with ε, leading to a decrease of f when the simulation cell is expanding. The onset void area fraction for the three regimes, as well as the simulation cell area evolution after the yield point, vary as e or θ changes.

We emphasize that this work with circular or elliptic voids lays a solid foundation for future work of the growth of ellipsoids, which requires more geometric parameters for characterization in larger 3-D simulation cells.

Acknowledgments

Appendix A.   Effect of the time step

To explore the effect of the time step Δt, we perform MD simulations with $\Delta t = 1$ fs in cases of the initially circular void and the elliptic voids of $e = 0.8$ with $\theta = 0°$, 45°, and 90°, respectively. All other simulation parameters, such as the strain rate and temperature, remain the same as when $\Delta t = 2$ fs. Figure A1(a) shows that for the same void, the difference in the yield stress between using 1 fs and 2 fs is less than 1%. Moreover, compared with the case of $\Delta t = 2$ fs, the defect nucleation and evolution at the void surface is almost identical when the time step is halved, as shown in figure A1(b).

Appendix B.   Asymmetry of the defects at the void surface

As presented in section 3.2, in all cases, the defects at the void surface are asymmetric with respect to the y axis. Below, take the elliptic void of $e = 0.8$ with $\theta = 90°$ as an example, we show that the asymmetry of the defects is related to the stochastic atomic trajectories in an NPT ensemble and the random atomic velocities initialization before the dynamic run.

First, to show that the NPT ensemble is a cause for the asymmetry, we perform an MD simulation with an NVE ensemble. The random number seed R_{seed} that is used in initializing
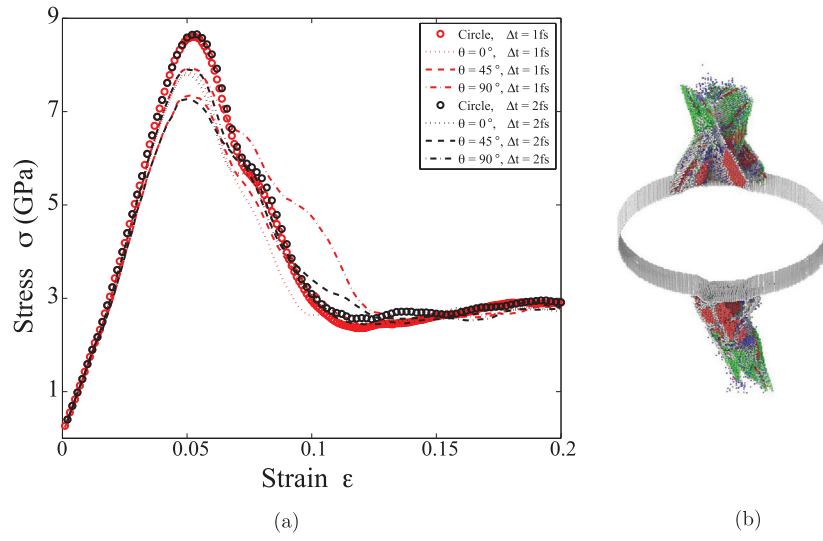
13

(a)   (b)

Figure A1. (a) Stress–strain curves for the initially circular void and elliptic voids of $e = 0.8$ with three different orientation angles θ when the time step $\Delta t = 1$ fs and 2 fs respectively. It is found that the Δt-dependent difference in the stress–strain response is trivial. (b) At $\varepsilon = 0.048$, the snapshot of defect at the surface of the elliptic void of $e = 0.8$ with $\theta = 0°$ when $\Delta t = 1$ fs is almost identical to that when $\Delta t = 2$ fs (figure 5(b)).
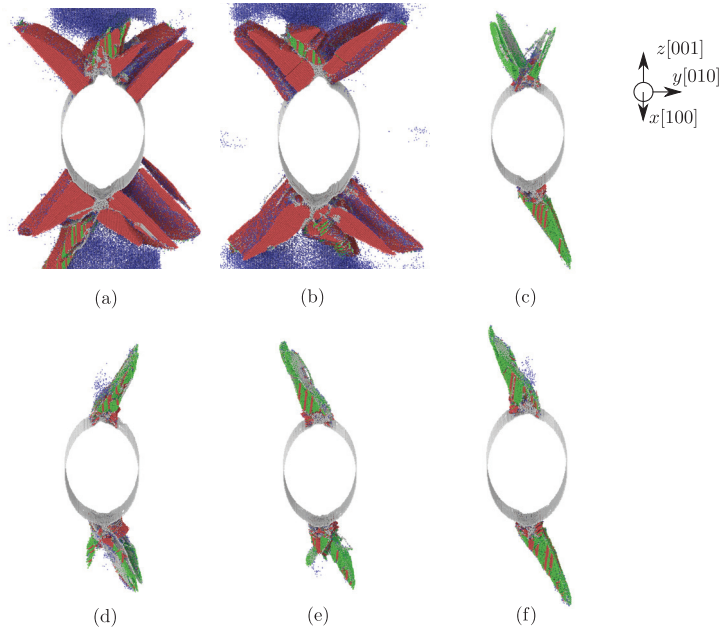

(a)   (b)   (c)

(d)   (e)   (f)

Figure B1. Snapshots of defect at the surface of the elliptic void of $e = 0.8$ with $\theta = 90°$ at $\varepsilon = 0.06$ with different ensemble and velocity initialization. (d) is the same as figure 7(d). (a) NVE ensemble without velocity initialization. (b) NVE ensemble with velocity initialization ($R_{\mathrm{seed}} = 1$). (c) NPT ensemble without velocity initialization. (d) NPT ensemble with velocity initialization ($R_{\mathrm{seed}} = 1$). (e) NPT ensemble with velocity initialization ($R_{\mathrm{seed}} = 2$). (f) NPT ensemble with velocity initialization ($R_{\mathrm{seed}} = 3$).

the atomic velocities before the dynamic run is 1, the same as in section 2. Note that with the NVE ensemble, the temperature is not constant and the lengths of the simulation cell along the x and z axes do not change during the tensile loading along the y direction. Figure B1(a) shows that the defects are asymmetric with respect to the y axis with an NVE ensemble, yet the defect configuration is different from that with an NPT ensemble (figure 7(d)). Second, to show that the random atomic velocities initialization might also lead to the asymmetry, we perform two MD simulations without initializing the atomic velocities with, respectively, an NVE or NPT ensemble. The defect is found to be asymmetric, yet with a different configuration, as shown in figures B1(b) and (c). In the end, to understand the influence of the random number seed R_{seed} on the defect configuration, we perform MD simulations at an NPT ensemble with three different $R_{seed} = 1$, 2, and 3, as shown in figures B1(d)–(f) respectively. It is found that the value of R_{seed} indeed affects the defect configuration.

References

[1] Bringa E M, Traiviratana S and Meyers M A 2010 Void initiation in fcc metals: effect of loading orientation and nanocrystalline effects *Acta Mater.* **58** 4458–77
[2] Besson J 2010 Continuum models of ductile fracture: a review *Int. J. Damage Mech.* **19** 3–52
[3] Xiong L, Xu S, McDowell D L and Chen Y 2015 Concurrent atomisticcontinuum simulations of dislocationvoid interactions in fcc crystals *Int. J. Plast.* **65** 33–42
[4] Xu S Z, Hao Z M, Su Y Q, Hu W J, Yu Y and Wan Q 2012 Atomic collision cascades on void evolution in vanadium *Radiat. Eff. Defects Solids* **167** 12–25
[5] Nakai R, Yabuuchi K, Nogami S and Hasegawa A 2016 The effect of voids on the hardening of body-centered cubic Fe *J. Nucl. Mater.* **471** 233–8
[6] Tang T, Kim S and Horstemeyer M F 2010 Molecular dynamics simulations of void growth and coalescence in single crystal magnesium *Acta Mater.* **58** 4742–59
[7] Deng X, Zhu W, Zhang Y, He H and Jing F 2010 Configuration effect on coalescence of voids in single-crystal copper under shock loading *Comput. Mater. Sci.* **50** 234–8
[8] Yerra S K, Teko C, Scheyvaerts F, Delannay L, Van Houtte P and Pardoen T 2010 Void growth and coalescence in single crystals *Int. J. Solids Struct.* **47** 1016–29
[9] Potirniche G P, Hearndon J L, Horstemeyer M F and Ling X W 2006 Lattice orientation effects on void growth and coalescence in fcc single crystals *Int. J. Plast.* **22** 921–42
[10] Ha S and Kim K T 2010 Void growth and coalescence in f.c.c. single crystals *Int. J. Mech. Sci.* **52** 863–73
[11] Tvergaard V 2011 Void shape effects and voids starting from cracked inclusion *Int. J. Solids Struct.* **48** 1101–8
[12] Seppälä E T, Belak J and Rudd R E 2004 Effect of stress triaxiality on void growth in dynamic fracture of metals: a molecular dynamics study *Phys. Rev.* B **69** 134101
[13] Traiviratana S, Bringa E M, Benson D J and Meyers M A 2008 Void growth in metals: atomistic calculations *Acta Mater.* **56** 3874–86
[14] Chang H-J, Segurado J, Rodríguez de la Fuente O, Pabón B M and LLorca J 2013 Molecular dynamics modeling and simulation of void growth in two dimensions *Modelling Simul. Mater. Sci. Eng.* **21** 075010
[15] Xu S Z, Hao Z M and Wan Q 2010 A molecular dynamics study of void interaction in copper *IOP Conf. Ser.: Mater. Sci. Eng.* **10** 012175
[16] Su Y and Xu S 2016 On the role of initial void geometry in plastic deformation of metallic thin films: a molecular dynamics study *Mater. Sci. Eng.* A **678** 153–64
[17] Cui Y and Chen Z 2016 Material transport via the emission of shear loops during void growth: a molecular dynamics study *J. Appl. Phys.* **119** 225102
[18] Potirniche G P, Horstemeyer M F, Wagner G J and Gullett P M 2006 A molecular dynamics study of void growth and coalescence in single crystal nickel *Int. J. Plast.* **22** 257–78
[19] Cui Y and Chen Z 2015 Molecular dynamics modeling on the role of initial void geometry in a thin aluminum film under uniaxial tension *Modelling Simul. Mater. Sci. Eng.* **23** 085011
[20] Zhang R F, Wang J, Beyerlein I J and Germann T C 2011 Twinning in bcc metals under shock loading: a challenge to empirical potentials *Phil. Mag. Lett.* **91** 731–40

[21] Queyreau S, Marian J, Gilbert M R and Wirth B D 2011 Edge dislocation mobilities in bcc Fe obtained by molecular dynamics *Phys. Rev.* B **84** 064106

[22] Cai W, Bulatov V V, Chang J, Li J and Yip S 2005 Dislocation core effects on mobility *Dislocations in Solids* vol 12, ed J P Hirth and F R N Nabarro (Amsterdam: Elsevier) pp 1–80

[23] Marichal C, Van Swygenhoven H, Van Petegem S and Borca C 2013 {1 1 0} Slip with {1 1 2} slip traces in bcc Tungsten *Sci. Rep.* **3** 2547

[24] Weinberger C R, Boyce B L and Battaile C C 2013 Slip planes in bcc transition metals *Int. Mater. Rev.* **58** 296–314

[25] Xu S Z, Hao Z M, Su Y Q, Yu Y, Wan Q and Hu W J 2011 An analysis on nanovoid growth in body-centered cubic single crystalline vanadium *Comput. Mater. Sci.* **50** 2411–21

[26] Rudd R E 2009 Void growth in bcc metals simulated with molecular dynamics using the Finnis–Sinclair potential *Phil. Mag.* **89** 3133–61

[27] Tang Y, Bringa E M, Remington B A and Meyers M A 2011 Growth and collapse of nanovoids in tantalum monocrystals *Acta Mater.* **59** 1354–72

[28] Tang Y, Bringa E M and Meyers M A 2012 Ductile tensile failure in metals through initiation and growth of nanosized voids *Acta Mater.* **60** 4856–65

[29] Cui Y and Chen Z 2015 Molecular dynamics simulation of the influence of elliptical void interaction on the tensile behavior of aluminum *Comput. Mater. Sci.* **108** 103–13

[30] Proville L, Rodney D and Marinica M-C 2012 Quantum effect on thermally activated glide of dislocations *Nat. Mater.* **11** 845–9

[31] Dezerald L, Rodney D, Clouet E, Ventelon L and Willaime F 2016 Plastic anisotropy and dislocation trajectory in BCC metals *Nat. Commun.* **7** 11695

[32] Plimpton S 1995 Fast parallel algorithms for short-range molecular dynamics *J. Comput. Phys.* **117** 1–19

[33] Stukowski A 2010 Visualization and analysis of atomistic simulation data with OVITO—the open visualization tool *Modelling Simul. Mater. Sci. Eng.* **18** 015012

[34] Stukowski A 2012 Structure identification methods for atomistic simulations of crystalline materials *Modelling Simul. Mater. Sci. Eng.* **20** 045021

[35] Su Y 2016 Void evolution www.prism.gatech.edu/~ysu65/codes/void/voids.html

[36] Towns J *et al* 2014 XSEDE: accelerating scientific discovery *Comput. Sci. Eng.* **16** 62–74

[37] Kelchner C L, Plimpton S J and Hamilton J C 1998 Dislocation nucleation and defect structure during surface indentation *Phys. Rev.* B **58** 11085–8

[38] Borodin V A and Vladimirov P V 2011 Molecular dynamics simulations of quasi-brittle crack development in iron *J. Nucl. Mater.* **415** 320–8

[39] Mendelev M I, Han S, Srolovitz D J, Ackland G J, Sun D Y and Asta M 2003 Development of new interatomic potentials appropriate for crystalline and liquid iron *Phil. Mag.* **83** 3977–94

[40] Ma L, Xiao S, Deng H and Hu W 2014 Molecular dynamics simulation of fatigue crack propagation in bcc iron under cyclic loading *Int. J. Fatigue* **68** 253–9

[41] Wang S J, Wang H, Du K, Zhang W, Sui M L and Mao S X 2014 Deformation-induced structural transition in body-centred cubic molybdenum *Nat. Commun.* **5** 3433

[42] Latapie A and Farkas D 2003 Molecular dynamics simulations of stress-induced phase transformations and grain nucleation at crack tips in Fe *Modelling Simul. Mater. Sci. Eng.* **11** 745–53

[43] Ekman M, Sadigh B, Einarsdotter K and Blaha P 1998 *Ab initio* study of the martensitic bcc-hcp transformation in iron *Phys. Rev.* B **58** 5296–304

[44] Machová A, Beltz G E and Chang M 1999 Atomistic simulation of stacking fault formation in bcc iron *Modelling Simul. Mater. Sci. Eng.* **7** 949–74

[45] Bulatov V V, Wolfer W G and Kumar M 2010 Shear impossibility: comments on 'void growth by dislocation emission' and 'void growth in metals: atomistic calculations' *Scr. Mater.* **63** 144–7

[46] Hirth J P and Lothe J 1992 *Theory of Dislocations* (Malabar, FL: Krieger Pub. Co.)

[47] Bringa E M, Lubarda V A and Meyers M A 2010 Response to 'shear impossibility—comments on 'void growth by dislocation emission' and 'void growth in metals' *Scr. Mater.* **63** 148–50

[48] Stukowski A, Bulatov V V and Arsenlis A 2012 Automated identification and indexing of dislocations in crystal interfaces *Modelling Simul. Mater. Sci. Eng.* **20** 085007

[49] Rabkin E and Srolovitz D J 2007 Onset of plasticity in gold nanopillar compression *Nano Lett.* **7** 101–7

[50] Möller J J and Bitzek E 2015 On the influence of crack front curvature on the fracture behavior of nanoscale cracks *Eng. Fract. Mech.* **150** 197–208